

Simulated observations of sub-millimetre galaxies: the impact of single-dish resolution and field variance

William I. Cowley*, Cedric G. Lacey, Carlton M. Baugh, Shaun Cole

Institute for Computational Cosmology, Department of Physics, University of Durham, South Road, Durham, DH1 3LE, UK.

3 December 2024

ABSTRACT

Recent observational evidence suggests that the coarse angular resolution ($\sim 20''$ FWHM) of single-dish telescopes at sub-mm wavelengths has biased the observed galaxy number counts by blending together the sub-mm emission from multiple sub-mm galaxies (SMGs). We use lightcones computed from an updated implementation of the GALFORM semi-analytic model to generate 50 mock sub-mm surveys of 0.5 deg^2 at $850 \mu\text{m}$, taking into account the effects of the finite single-dish beam in a more accurate way than has been done previously. We find that blending of SMGs does lead to an enhancement of source extracted number counts at bright fluxes ($S_{850\mu\text{m}} \gtrsim 1 \text{ mJy}$). Typically, ~ 4 galaxies contribute 90% of the flux of an $S_{850\mu\text{m}} = 5 \text{ mJy}$ source and these blended galaxies are physically unassociated. We find that field-to-field variations are comparable to Poisson fluctuations for our $S_{850\mu\text{m}} > 5 \text{ mJy}$ SMG population, which has a median redshift $z_{50} = 2.05$, but are greater than Poisson for the $S_{850\mu\text{m}} > 1 \text{ mJy}$ population ($z_{50} = 2.77$). In a detailed comparison with the ALESS survey we reproduce the difference between single-dish and interferometer number counts, as well as the high-redshift tail of the observed photometric redshift distribution and find a median redshift ($z_{50} = 2.58$) consistent with the observed value ($z_{50} = 2.5 \pm 0.2$). We also present predictions for single-dish survey number counts at 450 and $1100 \mu\text{m}$ which show good agreement with observational data.

Key words: galaxies: sub-millimetre

1 INTRODUCTION

One of the main goals of the study of galaxy formation and evolution is to understand the star formation history of the Universe. A key advance in this area was the discovery of the cosmic far-infrared extragalactic background light (EBL) by the *COBE* satellite (Puget et al. 1996; Fixsen et al. 1998) with an energy density similar to that of the UV/optical EBL, implying that a significant amount of star formation over the history of the Universe has been obscured and reprocessed by dust. Following this, the population of galaxies now generally referred to as sub-millimetre galaxies (SMGs) was first revealed using the Sub-millimetre Common User Bolometer Array (SCUBA) on the James Clerk Maxwell Telescope (JCMT) (e.g. Smail et al. 1997; Hughes et al. 1998). SMGs are relatively bright in sub-millimetre bands (the first surveys focussed on galaxies with $S_{850\mu\text{m}} > 5 \text{ mJy}$) and some studies have now shown that the bulk of the EBL at $850\mu\text{m}$ can be resolved by the $S_{850\mu\text{m}} > 0.1 \text{ mJy}$ galaxy population (e.g. Chen et al. 2013). SMGs are generally believed to be massive, dust enshrouded galaxies with extreme infrared luminosities ($L_{\text{IR}} \gtrsim 10^{12} L_{\odot}$) implying prodigious star formation rates (SFRs, 10^2 - $10^3 \text{ M}_{\odot} \text{ yr}^{-1}$), though this is heavily dependent on the assumed stellar initial mass function (IMF) (e.g. Blain et al. 2002; Casey et al. 2014).

One difficulty for sub-millimetre observations is the coarse angular resolution ($\sim 20''$ FWHM) of ground-based single-dish telescopes used for many blank-field surveys. Recently, follow-up surveys of single-dish detected sources performed with greater angular resolution ($\sim 1.5''$ FWHM) interferometers (e.g. Atacama Large Millimetre Array - ALMA, Plateau de Bure Interferometer - PdBI) have indicated that the resolution of single-dish telescopes had in some cases blended the sub-mm emission of multiple galaxies into one single-dish source (e.g. Wang et al. 2011; Smolčić et al. 2012; Hodge et al. 2013). Karim et al. (2013) showed the effect this blending has on the observed sub-mm number counts, with the single-dish counts derived from the Large Apex BOlometer Array (LABOCA) Extended Chandra Deep Field-South (ECDF-S) Sub-millimetre Survey (LESS, Weiß et al. 2009) exhibiting a significant enhancement at the bright end relative to counts derived from the ALMA follow-up (ALESS).

A related observational difficulty concerning SMGs is determining robust multi-wavelength counterparts for single-dish sources. This is in part due to the single-dish resolution spreading the sub-mm emission over a large solid angle making it difficult to pinpoint the precise origin to an accuracy of greater than $\pm 2''$. This process is also compounded by the faintness of SMGs at other wavelengths. Sub-mm bands are subject to a negative K -correction, which results in the sub-mm flux of an SMG being roughly constant over a large range of redshifts $z \sim 1 - 10$ (e.g.

* E-mail: w.i.cowley@durham.ac.uk

Blain et al. 2002). This negative K -correction is caused by the spectral energy distribution (SED) of a galaxy being a decreasing power law with wavelength where it is sampled by observer-frame sub-mm bands. As the SED is shifted to higher redshifts it is sampled at a shorter rest-frame wavelength, where it is intrinsically brighter. This largely cancels out the effect of dimming due to the increasing luminosity distance. When observed at other wavelengths e.g. radio, galaxies are subject to a positive K -correction and so become fainter with increasing redshift. This is problematic as radio emission has often been used to aid in measuring the position of the sub-mm source, as the star formation that powers the dust emission in the sub-mm also produces radio emission from synchrotron electrons produced by the associated supernovae explosions. This radio selection technique thus biases the counterpart identification towards lower redshift (e.g. Chapman et al. 2005). Typically, radio-identification yields robust counterparts for $\sim 60\%$ of an SMG sample (e.g. Biggs et al. 2011). Sub-mm interferometers have greatly improved the situation, providing positional accuracies of up to $\sim 0.2''$, free from any biases introduced by selection criteria at wavelengths other than the sub-mm. Once multi-wavelength counterparts have been identified, photometric redshifts are derived through fitting an SED to the available photometry, allowing redshift to vary as a free parameter (e.g. Smolčić et al. 2012). Whilst observationally inexpensive and thus desirable for large SMG surveys, the errors from photometric redshifts are often significant, and samples are again biased by requiring detection in photometric bands.

Compounding these difficulties is the fact that, with the exception of the South Pole Telescope (SPT) survey presented in Vieira et al. (2010)¹, sub-mm surveys have to date been pencil beams ($< 0.7 \text{ deg}^2$) leaving interpretation of the observed results subject to field-to-field variations. In particular, Michałowski et al. (2012) found evidence that photometric redshift distributions of radio-identified counterparts of 1100 and 850 μm selected SMGs in the two non-contiguous SCUBA Half-Degree Extragalactic Survey (SHADES) fields are inconsistent with being drawn from the same parent distribution. This suggests that the SMGs are tracing different large scale structures in the two fields.

Historically, hierarchical galaxy formation models have struggled to reproduce the high number density of the SMG population at high redshifts (e.g. Blain et al. 1999; Devriendt & Guiderdoni 2000; Granato et al. 2000). However Baugh et al. (2005) presented a version of the Durham semi-analytic model (SAM), GALFORM, which could successfully reproduce the observed number counts and redshift distribution of SMGs, along with the present day luminosity function. In order to do so it was found necessary to significantly increase the importance of high-redshift starbursts in the model; this was primarily achieved through introducing a top-heavy stellar initial mass function (IMF) for galaxies undergoing a (merger induced) starburst. Recently, Hayward et al. (2013) introduced a hybrid model which combined the results from idealized hydrodynamical simulations of isolated discs/mergers with various empirical cosmological relations and showed reasonable agreement with the 850 μm number counts and redshift distribution utilising a solar neighbourhood IMF. However, this model is limited in terms of the range of predictions it can make due to its semi-empirical

nature. A similar model was presented in Hayward et al. (2013) which included a treatment of blending by single dish telescopes, showing that the sub-mm emission from both physically associated and unassociated SMGs contribute significantly to the single-dish number counts. However, this model under predicts the observed single-dish number counts at $S_{850\mu\text{m}} > 5 \text{ mJy}$.

Here we investigate the effect of both the angular resolution of single-dish telescopes and field-to-field variations on observations of the SMG population. We utilise 50 randomly orientated lightcones calculated from an updated version of GALFORM (Lacey et al. 2014, in preparation, hereafter L14) to create mock sub-mm surveys taking into account the effects of the single-dish beam. This paper is structured as follows: in Section 2 we introduce the theoretical model we use for this analysis and our method for creating our 850 μm mock sub-mm surveys. In Section 3 we present our main results concerning the effects of the single-dish beam and field-to-field variance. In Section 4 we make a detailed comparison of the predictions of our model with the ALESS survey and in Section 5 we present our predicted single-dish number counts at 450 and 1100 μm . We summarise our findings and conclude in Section 6.

2 THE THEORETICAL MODEL

In this section we present the model used in this work. We couple a state-of-the-art semi-analytic galaxy formation model run in a Millennium-class (Springel et al. 2005) N -body simulation using the WMAP7 cosmology (Komatsu et al. 2011)², with a simple model for the re-processing of stellar radiation by dust (in which the dust temperature is calculated self-consistently). A sophisticated lightcone treatment is implemented for creating mock catalogues of the simulated galaxies (Merson et al. 2013). We also describe our method for creating sub-mm maps from these mock catalogues, which include the effects of the single-dish beam size and instrumental noise, from which we extract sub-mm sources in a way that is consistent with what is done in observational studies.

2.1 GALFORM

The Durham SAM, GALFORM, was first introduced in Cole et al. (2000). Galaxy formation is modelled *ab initio*, beginning with a specified cosmology and a linear power spectrum of density fluctuations and ending with predicted galaxy properties at a range of redshifts. Galaxies are assumed to form within dark matter halos, with their subsequent evolution controlled by the merging history of the halo. These halo merger histories can be calculated using a Monte Carlo technique following extended Press-Schechter formalism (Parkinson et al. 2008), or (as is the case in this work) extracted directly from N -body dark matter only simulations (e.g. Helly et al. 2003; Jiang et al. 2014). Baryonic physics is modelled as a set of continuity equations that track the exchange of baryons between stellar, cold disc gas and hot halo gas components. The main physical processes that are modelled include: (i) hierarchical assembly of dark matter halos; (ii) shock heating and virialization of gas in halo potential wells; (iii) radiative cooling and collapse of gas onto galactic discs; (iv) star formation from cold gas; (v) heating and expulsion of gas through feedback processes; (vi) chemical evolution of gas and stars; (vii) mergers of galaxies within halos due to

¹ These authors surveyed 87 deg^2 at 1.4 (2) mm to a depth of 11 (4.4) mJy with a $63''$ ($69''$) FWHM beam. Due to the flux limits and wavelength of this survey, the millimetre detections are mostly gravitationally lensed sources (Vieira et al. 2013).

² $\Omega_0 = 0.272$, $\Lambda_0 = 0.728$, $h = 0.704$, $\Omega_b = 0.0455$, $\sigma_8 = 0.81$, $n_s = 0.967$.

dynamical friction; (viii) evolution of stellar populations using stellar population synthesis (SPS) models; and (ix) the extinction and reprocessing of stellar radiation due to dust. As with other SAMs, the simplified nature of the equations that are used to characterise these complex and in some cases poorly understood physical processes introduce a number of parameters into the model. These parameters are constrained using a combination of simulation results and observational data, reducing enormously the available parameter space. In particular, the strategy of Cole et al. (2000) is that for a galaxy formation model to be deemed successful it must reproduce the present day ($z = 0$) luminosity function in optical and near infra-red bands. For a more detailed overview of SAMs see the reviews by Baugh (2006) and Benson (2010).

Several GALFORM models have appeared in the literature that adopt different values for the model parameters and in some cases include different physical processes. For this work we adopt the model presented in L14 because of its success at reproducing the number counts and redshift distribution of sub-mm galaxies at $850\mu\text{m}$. L14 combines a number of important physical processes from previous GALFORM models. These include the effects of AGN feedback inhibiting gas cooling in massive haloes (Bower et al. 2006), and a star formation law for galaxy discs (Lagos et al. 2011) based on an empirical relationship between the star formation rate and molecular-phase gas density (Blitz & Rosolowsky 2006). For the purposes of predicting sub-mm galaxies a top-heavy IMF is implemented for starbursts, as in Baugh et al. (2005). However, in L14 a much less extreme slope is needed compared to that invoked by Baugh et al.³. The top-heavy IMF enhances the sub-mm luminosity of a starbursting galaxy through a combination of an enhanced number of massive stars which increases the un-attenuated UV luminosity of the galaxy, and a greater number of supernovae events which increases the metal content and hence dust mass available to absorb and re-emit the stellar radiation at sub-mm wavelengths. A significant difference between Baugh et al. (2005) and L14 is that in Baugh et al. the starburst population was induced by galaxy mergers, whilst in L14 starbursts are primarily caused by disc instabilities. These instabilities use the same stability criterion for self-gravitating discs presented in Mo et al. (1998); Cole et al. (2000) and were included in Bower et al. (2006), but were not considered in Baugh et al. (2005). As with other GALFORM models, a standard Kennicutt (1983) IMF is adopted in L14 for quiescently star forming discs.

The model presented in L14 is designed to run in a Millennium-class dark matter only N -body simulation using a WMAP7 cosmology with a minimum halo mass of $10^{10} M_\odot$. This work uses 50 output snapshots from the model, spaced approximately linearly with time in the redshift range $z = 0$ -8.5, we use this large redshift range so that our simulated SMG population is complete.

2.2 The Dust Model

In order for the sub-mm flux of galaxies to be predicted, a model is required to calculate the amount of stellar radiation absorbed by dust and the resulting SED of the dust emission. Here we use a model motivated by the radiative transfer code GRASIL (Silva et al. 1998). GRASIL calculates the heating and cooling of dust grains of varying sizes and compositions at different locations within each

galaxy, effectively obtaining the dust temperature T_d at each position. GRASIL has been coupled with GALFORM in previous works (e.g. Granato et al. 2000; Baugh et al. 2005; Swinbank et al. 2008). However, due to the computational expense of running GRASIL for the number of GALFORM galaxies generated in the simulation volume used in this work, we use a model which retains some of the key assumptions of GRASIL but with a significantly simplified calculation. Despite the simplifications made this model can accurately reproduce the predictions of GRASIL for $\lambda_{\text{rest}} > 70 \mu\text{m}$, which is typically beyond the peak of the dust emission SED. We are therefore confident in its application to the wavelengths under investigation here. We briefly describe our dust model in the following section. However, for a more detailed explanation we refer the reader to the appendix of L14.

We adopt the GRASIL assumptions regarding the geometry of the stars and dust. Stars are distributed throughout two components (i) a spherical bulge with an $r^{1/4}$ density profile, and (ii) a flattened component which is either a quiescent disc or a starburst component, with exponential radial and vertical density profiles. Young stars and dust are assumed to be in the flattened component only. A two phase dust medium is also adopted, as in GRASIL. Dust and gas exist in either dense molecular clouds, modelled as uniform density spheres of fixed mass ($10^6 M_\odot$) and radius (16 pc), or a diffuse inter-cloud medium. Stars are assumed to form inside the molecular clouds and gradually escape into the diffuse dust on a timescale of a few Myrs, parametrised as t_{esc} in the model. The dust emission is first obtained by calculating the energy from stellar radiation absorbed in each dust component. Assuming thermal equilibrium, this is then equated to the energy emitted by the respective dust component such that the luminosity per unit wavelength emitted by a mass M_d of dust is given by

$$L_\lambda^{\text{dust}} = 4\pi\kappa_d B_\lambda(T_d)M_d, \quad (1)$$

where κ_d is the absorption cross-section per unit mass and $B_\lambda(T_d)$ is the Planck blackbody function. Crucially this means that T_d of each component is not a free parameter but is calculated self-consistently. An important simplifying assumption here is that we assume only two dust temperatures, one for the molecular clouds and one for the diffuse medium. The dust mass, M_d , is equivalent to the metallicity times the cold gas mass. The dust absorption cross-section per unit mass of metals in the gas phase is approximated as follows:

$$\kappa_d(\lambda) = \begin{cases} \kappa_1 \left(\frac{\lambda}{\lambda_1}\right)^{-2} & \lambda < \lambda_b \\ \kappa_1 \left(\frac{\lambda_b}{\lambda_1}\right)^{-2} \left(\frac{\lambda}{\lambda_b}\right)^{-\beta_b} & \lambda > \lambda_b, \end{cases} \quad (2)$$

where $\kappa_1 = 140 \text{ cm}^2 \text{ g}^{-1}$ at the reference wavelength $\lambda_1 = 30 \mu\text{m}$ (e.g. Draine & Lee 1984). The power-law break is introduced at $\lambda_b = 100 \mu\text{m}$ for starburst galaxies *only* (Silva et al. 1998), for quiescently star forming galaxies $\lambda_b \rightarrow \infty$ (an unbroken power law). A value of $\beta_b = 1.5$ is chosen.

The sub-mm number counts can be calculated by first constructing luminosity functions $dn/d\ln L_\nu$ at a given output redshift using L_ν calculated by the dust model. The binning is chosen so that we have fully resolved the bright end, to which the derived number counts are sensitive. The number counts and redshift distribution can then be calculated according to

$$\frac{d^2 N}{d\ln S_\nu dz d\Omega} = \left\langle \frac{dn}{d\ln L_\nu} \right\rangle \frac{dV}{dz d\Omega}, \quad (3)$$

where $dV/dz = (c/H(z))r^2(z)$ and the brackets $\langle \dots \rangle$ represent a

³ The slope of the IMF, x , in $dN(m)/d\ln m = m^{-x}$, has a value of $x = 1$ in L14 whereas a value of $x = 0$ was used in Baugh et al. (2005).

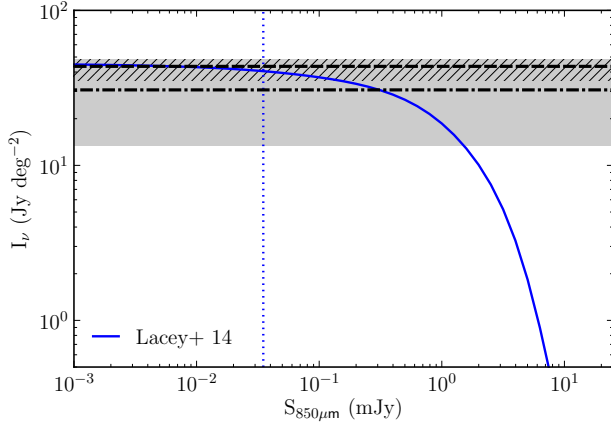


Figure 1. Cumulative extragalactic background light as a function of flux at $850\ \mu\text{m}$. The dashed line (Fixsen et al. 1998) and dashed-dotted line (Puget et al. 1996) show the background light as measured by the *COBE* satellite. The shaded (Puget et al. 1996) and hatched (Fixsen et al. 1998) regions indicate the respective errors on the two measurements. The vertical dotted line indicates the flux limit above which 90% of the total predicted EBL is resolved.

volume-averaging utilising the whole N -body simulation volume ($500\ h^{-1}\text{Mpc}$)³.

2.3 Creating mock surveys

In order to create mock catalogues of our sub-mm galaxies we utilise the lightcone treatment described in Merson et al. (2013). Briefly, as the initial simulation volume side-length ($L_{\text{box}} = 500\ h^{-1}\text{Mpc}$) corresponds to the co-moving distance out to $z \sim 0.17$ the simulation is periodically replicated in order to fully cover the volume of a typical SMG survey, which extends to much higher redshift. This replication could result in structures appearing to be repeated within the final lightcone which could produce unwanted projection-effect artefacts if their angular separation on the ‘mock sky’ is small (Blaizot et al. 2005). As our fields are small in solid angle ($0.5\ \text{deg}^2$) and our box size is large we expect this effect to be of negligible consequence and note that we have seen no evidence of projection-effect artefacts in our mock sub-mm maps. Once the simulation volume has been replicated, a geometry is determined by specifying an observer location and orientation. An angular cut defined by the desired solid angle of our survey is then applied, such that the mock survey area resembles a sector of a sphere. The redshift of a galaxy in the lightcone is calculated by first determining the redshift (z) at which its host dark matter halo enters the observer’s past lightcone. The positions of galaxies are then interpolated from the simulation output snapshots (z_i, z_{i+1} , where $z_{i+1} < z < z_i$) such that the real-space correlation function of galaxies is preserved. A linear K -correction interpolation is applied to the luminosity of the galaxy to account for the shift in $\lambda_{\text{rest}} = \lambda_{\text{obs}}/(1+z)$ for a given λ_{obs} , based on its interpolated redshift.

To create the $850\ \mu\text{m}$ mock catalogues we apply a further selection criterion to our galaxies of $S_{850\mu\text{m}} > 0.035\ \text{mJy}$. This is the limit brighter than which we recover $\sim 90\%$ of the $850\ \mu\text{m}$ EBL, as predicted by our model (Fig. 1). We have checked that our simulated SMG population is not affected by incompleteness at this low flux limit, due to the finite halo mass resolution of the N -body simulation. To allow us to test field-to-field variance we generate

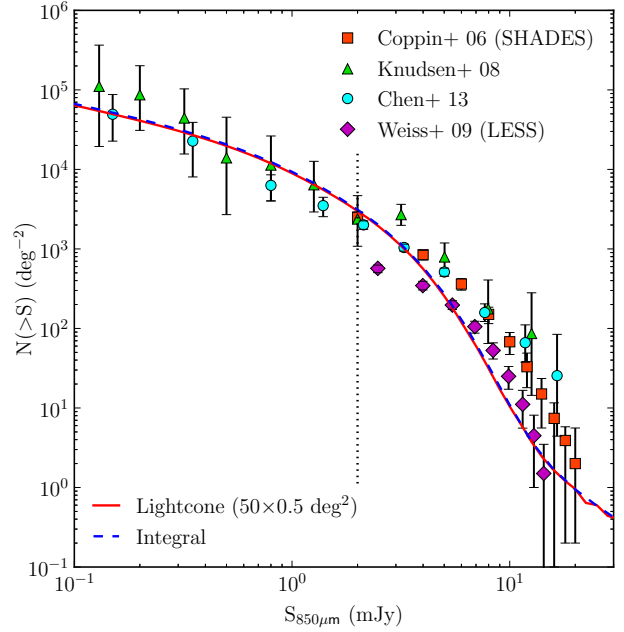


Figure 2. Cumulative number counts at $850\ \mu\text{m}$. Predictions from the lightcone catalogues and the integrated luminosity functions of the model are in excellent agreement. We compare the model predictions to single-dish observational data from Coppin et al. (2006) (orange squares), Knudsen et al. (2008) (green triangles), Weiß et al. (2009) (magenta diamonds) and Chen et al. (2013) (cyan circles). The vertical dotted line shows the approximate confusion limit ($\sim 2\ \text{mJy}$) of single-dish blank field surveys. Data fainter than this limit are derived from lensed cluster surveys (see Section 3.1 for further discussion).

$50 \times 0.5\ \text{deg}^2$ lightcone surveys⁴ with random observer positions and lines of sight. In Fig. 2 we show that the lightcone can very accurately reproduce the SMG population of our model.

2.4 Creating sub-mm maps

Here we describe the creation of mock sub-mm maps from our lightcone catalogues. First, we create an image by assigning the $850\ \mu\text{m}$ flux of a galaxy to the pixel in which it is located, using a pixel size much smaller than the single-dish beam. This image is then convolved with a point spread function (PSF), modelled as a 2D Gaussian with a $15''$ FWHM (\sim SCUBA2/JCMT), and then re-binned into a coarser image with $2'' \times 2''$ pixels, to match observational pixel sizes. The resulting image is then scaled so that it is in units of mJy/beam. We refer to the output of this process as the astrophysical map (see Fig 3a).

In order to better mimic the noise properties of observational maps we add ‘instrumental’ Gaussian noise to the astrophysical map. We tune the standard deviation of this noise such that after it has been matched-filtered (described below) the output is a noise map with $\sigma_{\text{rms}} \sim 1\ \text{mJy/beam}$, comparable to jackknifed noise maps in $850\ \mu\text{m}$ observational blank-field surveys (e.g. Coppin et al. 2006; Weiß et al. 2009; Chen et al. 2013).

It is a well known result in astronomy that the best way to find point-sources in the presence of noise is to convolve with the PSF

⁴ In practise our surveys are $0.55\ \text{deg}^2$. This allows for galaxies outside the $0.5\ \text{deg}^2$ area to contribute to sources detected inside this area after convolution with the single dish beam.

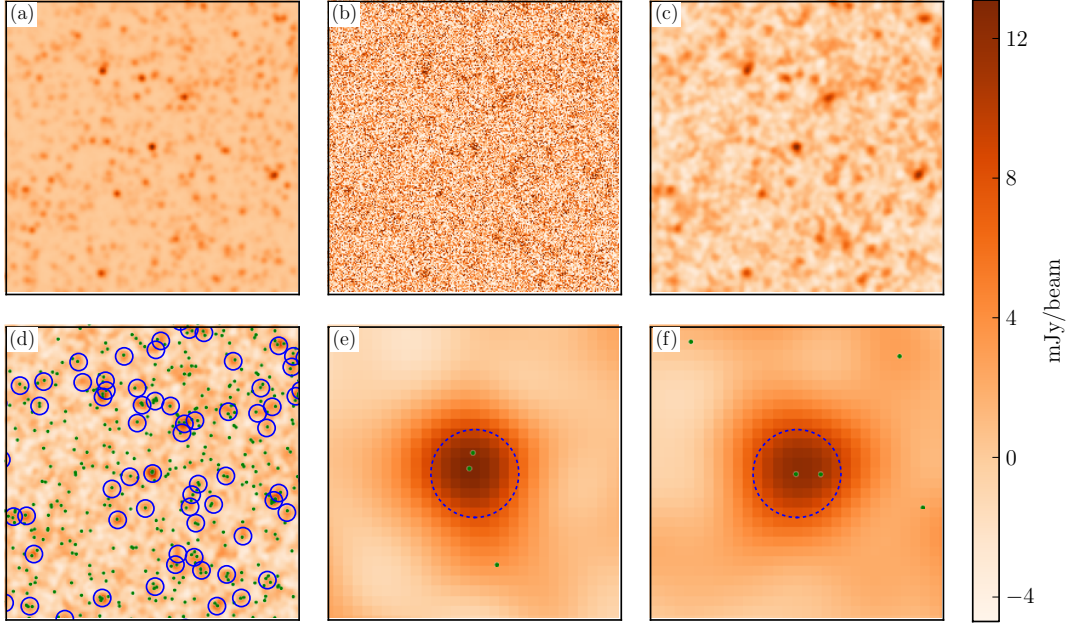


Figure 3. Panels illustrating the mock map creation process at $850\ \mu\text{m}$. Panels (a)-(d) are $0.2 \times 0.2\ \text{deg}^2$ and are centred on a 13.1 mJy source. (a) Astrophysical map. (b) Astrophysical plus Gaussian noise map, constrained to have zero mean. (c) Matched-filtered map. (d) Matched-filtered map with $S_{850\mu\text{m}} > 4\ \text{mJy}$ single-dish sources ($21.2''$ radius blue circles centred on the source position) and $S_{850\mu\text{m}} > 1\ \text{mJy}$ galaxies (green dots) overlaid. (e) As for (d) but for a $0.5' \times 0.5'$ area. The 2 galaxies within the $9''$ radius (dotted line, \sim ALMA primary beam) of the source have fluxes of 1.2 and 11.2 mJy and redshifts of 1.0 and 2.0 respectively. (f) as for (e) but centred on a 12.2 mJy source. In this case the 2 galaxies within the central $9''$ radius have fluxes of 6.1 and 6.4 mJy and redshifts of 2.0 and 3.2 respectively.

(Stetson 1987). However, this is only optimal if the noise is Gaussian and does not take into account ‘confusion noise’ from other point-sources. Chapin et al. (2011) show how one can optimise filtering for maps with significant confusion, through modelling this as a random (and thus un-clustered) superposition of point sources convolved with the PSF, normalised to the number counts inferred from $P(D)$ analysis of the maps. The PSF is then divided by the power spectrum of this confusion noise realisation. This results in a matched-filter with properties similar to a ‘Mexican-hat’ kernel. An equivalent method is implemented in Laurent et al. (2005). Although our simulated maps contain a significant confusion background, for simplicity we do not implement such a method here, and have checked that the precise method of filtering does not affect our results.

Prior to source extraction, we constrain our astrophysical plus Gaussian noise map to have a mean of zero (Fig. 3b) and convolve with a matched-filter $g(x)$, given by

$$g(x) = \mathcal{F}^{-1} \left\{ \frac{s^*(q)}{\int |s(q)|^2 d^2q} \right\}, \quad (4)$$

where \mathcal{F}^{-1} denotes an inverse Fourier transform, $s(q)$ is the Fourier transform of our PSF and the asterisk indicates complex conjugation. The denominator is the appropriate normalisation such that peak heights of PSF-shaped sources are preserved after filtering. Up to this normalisation factor, the matched-filtering is equivalent to convolving with the PSF. Point sources are therefore effectively convolved with the PSF twice, once by the telescope and once by the matched-filter. This gives our final matched-filtered map (Fig. 3c) a spatial resolution of $\sim 21.2''$ FWHM i.e. $\sqrt{2} \times 15''$.

For real surveys, observational maps often have large scale filtering applied prior to the matched-filtering described above. This is to remove large scale structure from the map, often an artefact of

correlated noise of non-astrophysical origin. This is implemented by convolving the map with a Gaussian broader than the PSF and then subtracting this off the original, rescaling such that the flux of point sources is conserved (e.g. Weiß et al. 2009; Chen et al. 2013). As our noise is Gaussian, any excess in the power spectrum of the map on large scales can only be attributed to our astrophysical signal, so we choose not to implement any such high-pass filtering prior to our matched-filtering.

An example of one of our matched-filtered maps is shown in Fig. 4 and the associated pixel histogram in Fig. 5. The position of the peak of the pixel histogram is determined by the constraint that our maps have a zero mean after subtracting a uniform background.

For the source extraction we first identify the peak (i.e. brightest) pixel in the map. For simplicity we record the source position and flux to be the centre and value of this peak pixel. We then subtract the matched-filtered PSF, scaled and centred on the value and position of the peak pixel, from our map. This process is iterated down to an arbitrary threshold value of $S_{850\mu\text{m}} = 1\ \text{mJy}$, resulting in our source-extracted catalogue.

3 RESULTS

In this section we present our main results: in Section 3.1 we show the effect the single-dish beam has on the predicted number counts through blending the sub-mm emission of galaxies into a single source. In Section 3.2 we quantify the multiplicity of blended sub-mm sources, in Section 3.3 we show that these blended galaxies are typically physically unassociated and in Section 3.4 we present the redshift distribution of our model.

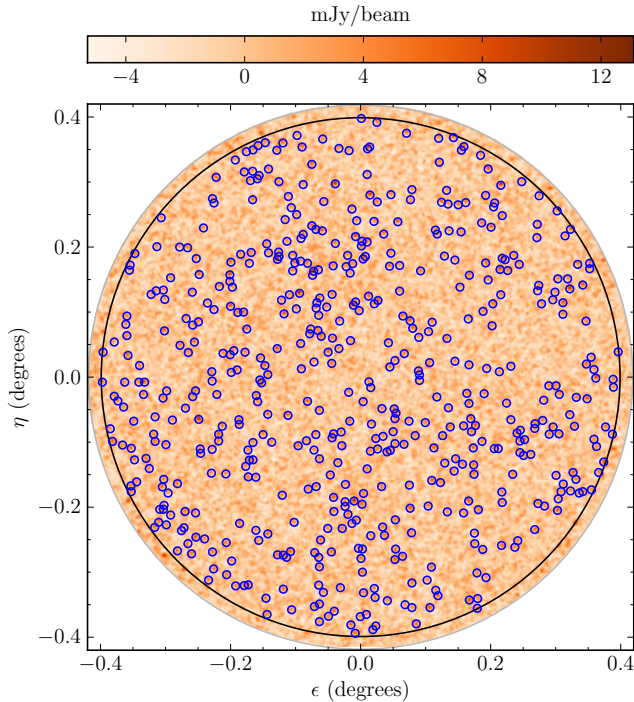


Figure 4. A matched-filtered map. Sources detected with $S_{850\mu\text{m}} > 4$ mJy by our source extraction algorithm are indicated by blue ($21.2''$ radius) circles. The central 0.5 deg^2 region, from which we extract our sources, is indicated by the black circle.

3.1 Number counts

The cumulative number counts derived from our lightcone and source-extracted catalogues are presented in Fig. 6. The shaded regions, which show the 10-90 percentiles of the distribution of number counts from the individual fields, give an indication of the field-to-field variation we predict for fields of 0.5 deg^2 area. This variation is comparable to (or less than) the quoted observational errors. A clear enhancement in the source-extracted number counts relative to those derived from our lightcone catalogues is evident at $S_{850\mu\text{m}} \gtrsim 1 \text{ mJy}$. We attribute this to the finite angular resolution of the beam blending together the flux from multiple galaxies with projected on-sky separations comparable to or less than the size of the beam. Our source-extracted number counts show better agreement with blank-field single-dish observational data above the confusion limit ($S_{\text{lim}} \approx 2 \text{ mJy}$) of such surveys, indicated by the vertical dotted line in Fig 6.

Observational data fainter than this limit have been measured from gravitationally lensed cluster fields, where gravitational lensing due to a foreground galaxy cluster magnifies the survey area, typically by a factor of a few, but up to ~ 20 . The magnification increases the effective angular resolution of the beam, thus reducing the confusion limit of the survey and the instances of blended galaxies. The lensing also boosts the flux of the SMGs. These effects allow cluster-lensed surveys to probe much fainter fluxes than blank-field surveys performed with the same telescope. We show observational data in Fig. 2 at $S_{850\mu\text{m}} < 2 \text{ mJy}$ for comparison with our lightcone catalogue number counts, with which they agree well.

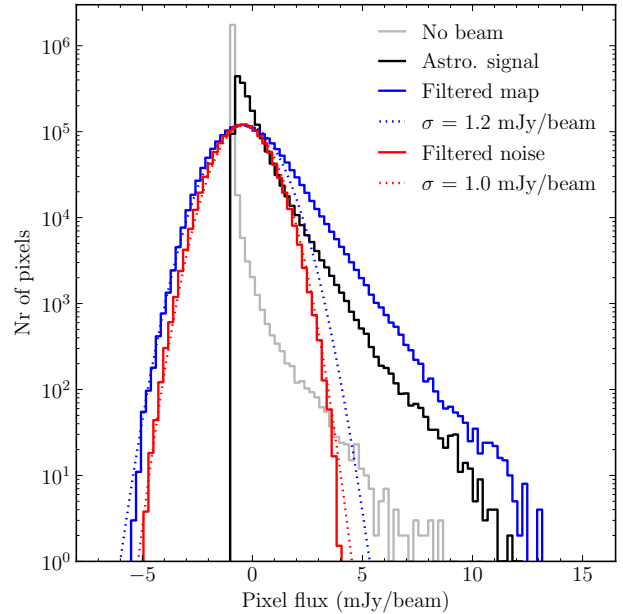


Figure 5. Pixel flux histogram of the map shown in Fig. 4. The grey and black lines are the map before and after convolution with the single-dish beam respectively, with the same zero point subtraction applied as to our final matched-filtered map (blue line). The map is rescaled after convolution with the single-dish beam to convert to units of mJy/beam (grey to black), and during the matched-filtering due to the normalisation of filter which conserves point source peaks (black to blue). Our matched-filtered noise-only map (red line) is constrained to have the same peak as the matched-filtered map. Dotted lines show Gaussian fits to the noise-only (red) and matched-filtered (blue) maps respectively.

3.2 Multiplicity of single-dish sources

Given that multiple SMGs can be blended into a single source, we quantify this multiplicity as follows: for each galaxy within a $21.2''$ radius⁵ of a given $S_{850\mu\text{m}} > 2 \text{ mJy}$ source, we determine the $850 \mu\text{m}$ flux of that galaxy at the source position, modelling the galaxy's flux distribution as a Gaussian with a peak value equal to the flux of the galaxy and a FWHM of $21.2''$. We label the sum of this as the total galaxy flux of the source. For each source we then interpolate the cumulative distribution after sorting in order of decreasing flux contribution to determine how many galaxies are required to contribute a given percentage of this total.

We plot this as a function of source-extracted flux, which includes the effect of instrumental noise, in the top 4 panels of Fig 7. Typically, 90% of the total galaxy flux of a 5 mJy source is contributed by ~ 4 galaxies and this multiplicity decreases slowly as source flux increases. This follows intuitively from the steep decrease in number density with increasing flux in the number counts. Studies which suggest that the multiplicity of sources may increase with increasing source flux (e.g. Hodge et al. 2013) are likely to be affected by a combination of the flux limit of the interferometer, meaning high multiplicity faint sources, are undetected and small numbers of bright sources.

⁵ We choose this radius as it is the the FWHM of our matched-filtered PSF, which is a factor $\sqrt{2}$ greater than the telescope beam PSF. Galaxies outside this radius will contribute $< 6.25\%$ of their flux and so make a negligible contribution to the source flux. This choice of radius does not qualitatively affect our results.

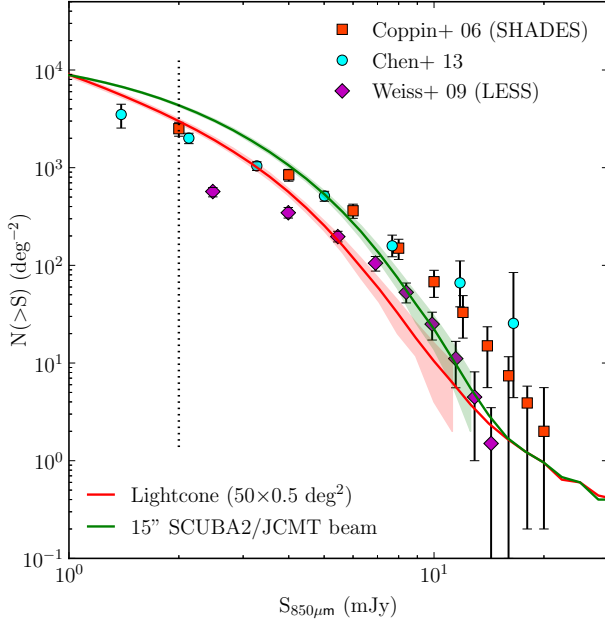


Figure 6. The effect of single-dish beam size on cumulative $850\ \mu\text{m}$ number counts. The shaded regions show 10-90 percentiles of the distribution of the number counts from the 50 individual fields, solid lines show counts from the combined $25\ \text{deg}^2$ field for the lightcone (red) and the $15''$ FWHM beam source extracted (green) catalogues. The vertical dotted line at $S_{850\mu\text{m}} = 2\ \text{mJy}$ indicates the approximate confusion limit of single-dish surveys. The $15''$ beam prediction is only to be compared at fluxes above this limit. Single-dish blank field observational data is taken from Coppin et al. (2006) (orange squares) Weiß et al. (2009) (magenta diamonds) and Chen et al (2013) (cyan circles).

We also show, in the bottom panel of Fig. 7, the ratio of the total galaxy flux to source flux. The consistency with zero indicates that our source-extracted number counts at $850\ \mu\text{m}$ are not systematically affected by flux boosting/Eddington bias. Eddington bias arises as the steepness of the number counts implies it is more likely that a source extracted flux S_{source} arises from intrinsic fluxes $S < S_{\text{source}}$ more often than from $S > S_{\text{source}}$. Observational surveys (e.g. Weiß et al. 2009) often find flux de-boosting at $850\ \mu\text{m}$ necessary to correct for this. However, this relies on fitting an assumed functional form for the differential number counts to the pixel histogram of the map. From this a source population is generated using Monte Carlo methods which is then injected into the jackknifed noise maps. For a given source, the flux determined by the source extraction is then compared to the input flux from the Monte Carlo population, revealing a systematic boosting at low fluxes due to the instrumental noise. Here, the number counts derived from source extraction performed on the astrophysical maps are equivalent to the best-fit functional forms derived observationally. We find that at $2\ \text{mJy}$ (2σ) the slope of our astrophysical maps source-extracted number counts is much less steep than the slope of the observed best-fit single power law model of Weiß et al. (2009), despite the fact that we agree with the data above the source extraction limit of the survey ($\sim 4.5\ \text{mJy}$), and so it is unsurprising that we conclude we are less affected by Eddington bias.

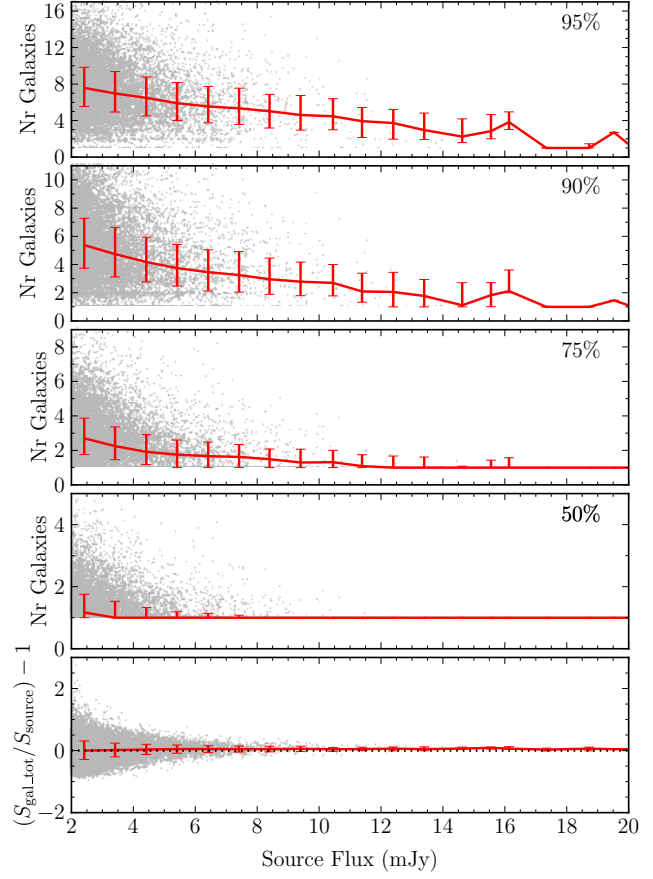


Figure 7. *Top 4 panels:* Number of component galaxies contributing the percentage indicated in the panel of the total galaxy flux (see text) of a $S_{850\mu\text{m}} > 2\ \text{mJy}$ source. *Bottom panel:* Ratio of total galaxy flux to source flux. Black dashed line is a reference line drawn at zero. Solid red line shows median and errorbars indicate inter-quartile range in all panels. For clarity only 10% of the sources have been plotted.

3.3 Physically unassociated galaxies

Given the multiplicity of our sources, we can further determine if the blended galaxies contributing to a source are physically associated, or if their blending has occurred due to a chance line of sight projection. For each source we define a redshift separation, Δz , as the inter-quartile range of the histogram of flux weighted redshifts the galaxies within an $21.2''$ radius of the source position. The flux weight (i.e. the flux of each galaxy at the source position) is calculated as described above. The distribution of Δz across our entire $S_{850\mu\text{m}} > 4\ \text{mJy}$ source population is shown in Fig. 8. The dominant peak at $\Delta z \approx 1$ (where the distribution peaks for a set of maps which have had the positions of SMGs randomised) suggests that our sources are predominantly composed of physically unassociated galaxies that have a small on-sky separation due to chance line of sight projection. We leave this as a prediction to be tested by future unbiased spectroscopic redshift surveys of SMGs (e.g. Danielson et al., in preparation).

It is a feature of most current SAMs that any star formation enhancement caused by gravitational interactions of physically associated galaxies prior to a merger event is not included. This may affect our physically unassociated prediction, as in our model galaxy mergers would only become sub-mm bright post merger, and would be classified as a single galaxy. However, as merger in-

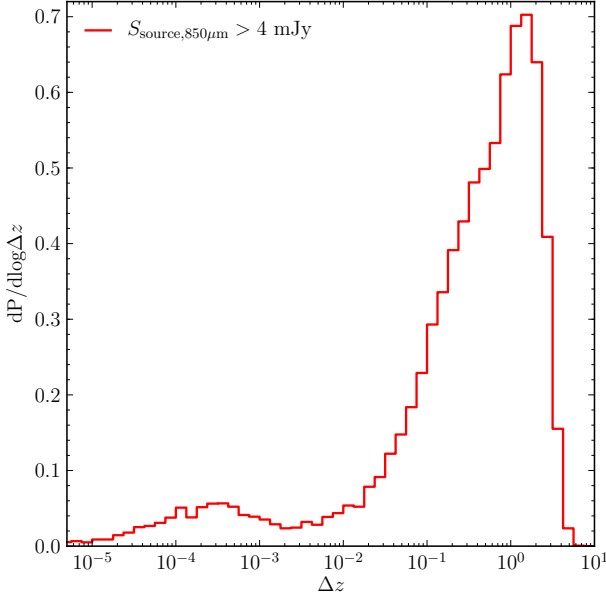


Figure 8. Distribution of the logarithm of redshift separation (see text) of $S_{850\mu\text{m}} > 4$ mJy single-dish sources. The dominant peak at $\Delta z \approx 1$ suggests that the majority of the blended galaxies are physically unassociated.

duced starbursts have a negligible effect on our sub-mm number counts, which are composed of starbursts triggered by disc instabilities (L14), we are confident our physically unassociated conclusion is not affected by this feature.

We note that this conclusion is in contrast to predictions made by Hayward et al. (2013) who, in addition to physically unassociated blends, predict a more significant physically associated population than is presented here. However, we believe our work has a number of significant advantages over that of Hayward et al. (2013) in that: (i) galaxy formation is modelled here *ab initio* with a model that can also successfully reproduce the present day galaxy luminosity function; (ii) the treatment of blending presented here is more accurate through convolution with a beam, the inclusion of instrumental noise and matched-filtering, rather than a summation of SMG flux within some radius around a given SMG; and (iii) our $15''$ source-extracted number counts show better agreement with single-dish data for $S_{850\mu\text{m}} \gtrsim 5$ mJy.

3.4 Redshift distribution

The redshift distributions for the ‘bright’ $S_{850\mu\text{m}} > 5$ mJy and ‘faint’ $S_{850\mu\text{m}} > 1$ mJy SMG populations are shown in Fig. 9. The shaded region shows the 16–84 (1σ) percentiles of the distributions from the 50 individual fields, arising from field-to-field variations. The errorbars indicate the 1σ Poisson errors. The bright SMG population has a lower median redshift ($z_{50} = 2.05$) than the faint one ($z_{50} = 2.77$). We note that the median redshift appears to be a robust statistic with an inter-quartile range of 0.17 (0.11) for the bright (faint) population for the 0.5 deg^2 field size assumed. The field-to-field variation seen in the bright population is comparable to the Poisson errors and thus random variations, whereas this field-to-field variation is greater (compared to Poisson) for the faint population. In order to further quantify this field-to-field variance we have performed the Kolmogorov-Smirnoff test between the 1225 combinations of our 50 fields, for the bright and faint populations.

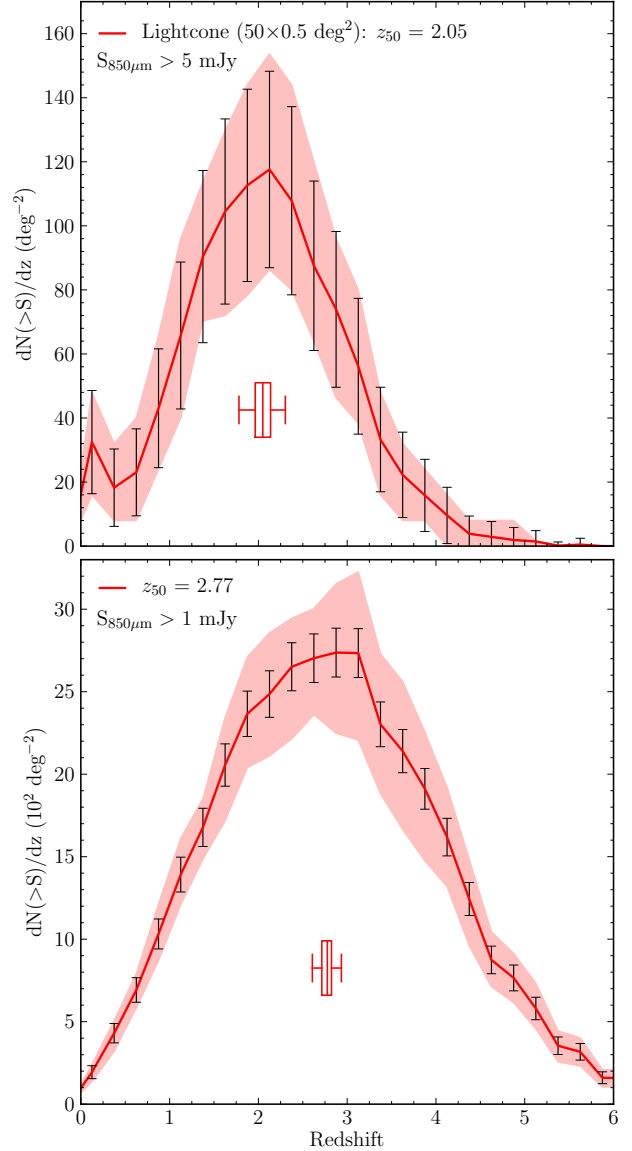


Figure 9. The predicted redshift distribution for our $50 \times 0.5 \text{ deg}^2$ fields for the flux limit indicated on each panel. The shaded red region shows the 16–84 (1σ) percentile of the distributions from the 50 individual fields. The solid red line is the distribution for the combined 25 deg^2 field. The boxplots represent the distribution of the median redshifts of the 50 fields, the whiskers show the full range, with the box and central line indicating the inter-quartile range and median. The errorbars show the expected 1σ variance due to Poisson errors.

We find that for the bright population the distribution of p -values is similar to that obtained if we perform the same operation with 50 random samplings of the parent field, though with a slightly more significant low p -value tail. Approximately 10% of the field pairs exhibit $p < 0.05$, suggesting that it is not necessarily as uncommon as one might expect by chance to find that redshift distributions derived from non-contiguous pencil beams of sky fail the K-S test, as in Michałowski et al. (2012). For the faint population, 92% of the field pairs have $p < 0.05$.

Thus, it appears that the bright population in the individual fields is more consistent with being a random sampling of the parent 25 deg^2 distribution. This is due to: (i) the number density of the

faint population being ~ 30 times greater than the bright population, which significantly reduces the Poisson errors; and (ii) the median halo mass of the two populations remaining similar, $7.6 (5.5) \times 10^{11} h^{-1} M_{\odot}$ for our bright (faint) population indicating that the two populations trace the underlying matter density with a similar bias. We consequently predict that as surveys probe the SMG population down to fainter fluxes we expect that they become more sensitive to field-to-field variations induced by large scale structure.

4 COMPARISON TO ALESS

In this section we make a detailed comparison of our model with observational data from the recent ALMA follow-up survey (Hodge et al. 2013) of LESS (Weiß et al. 2009), referred to as ALESS. LESS is an $870\mu\text{m}$ LABOCA ($19.2''$ FWHM) survey of 0.35 deg^2 (covering the full area of the E-CDFS) with a typical noise level of $\sigma \sim 1.2 \text{ mJy/beam}$. Weiß et al. (2009) extracted 126 sources based on a $S/N > 3.7\sigma$ ($\simeq S_{870\mu\text{m}} > 4.5 \text{ mJy}$) at which they were $\sim 70\%$ complete. Of these 126 sources, 122 were targeted for cycle 0 observations with ALMA. From these 122 maps, 88 were selected as ‘good’ based on their rms noise and axial beam ratio, from which 99 sources were extracted down to $\sim 1.5 \text{ mJy}$. The catalogue containing these 99 sources is presented in Hodge et al. (2013), with the resulting number counts and photometric redshift distribution being presented in Karim et al. (2013) and Simpson et al. (2013) respectively. For the purposes of our comparison we randomly sample (without replacement) 70% ($\sim 88/126$) of our $S_{850\mu\text{m}} > 4.5 \text{ mJy}$ sources from the central 0.35 deg^2 of our 50 mock maps⁶. Around all of our remaining sources we place $18''$ diameter masks (\sim ALMA primary beam) from which we extract our ‘follow-up’ galaxies down to $S_{850\mu\text{m}} = 1.5 \text{ mJy}$ from the relevant lightcone catalogue. The result of this being our ‘follow-up’ catalogue.

4.1 Number counts

We present the number counts from our simulated follow-up catalogues in Fig. 10 and observe a similar difference between our simulated single-dish and follow-up number counts as the (A)LESS survey found in their observed analogues (Weiß et al. 2009 and Karim et al. 2013 respectively). Also evident is the bias inherent in our simulated follow-up compared to our lightcone catalogues at fluxes fainter than the source extraction limit of the single-dish survey. This arises because follow-up galaxies are only selected due to their on-sky proximity to a single-dish source so they are not representative of a blank-field population. For this reason Karim et al. (2013) do not present number counts fainter than the source extraction limit of LESS, despite the ability of ALMA to probe fainter fluxes.

We compare the multiplicity of the observed ALESS sample with our simulated follow-up sample in Fig. 11. The ratio of the brightest follow-up galaxy flux for each source to the source flux is in excellent agreement with the observed sample, with the brightest of our follow-up galaxies being roughly 70% of the source flux on average. This fraction is roughly constant over the range of source fluxes probed by LESS. The scatter of our simulated data is also

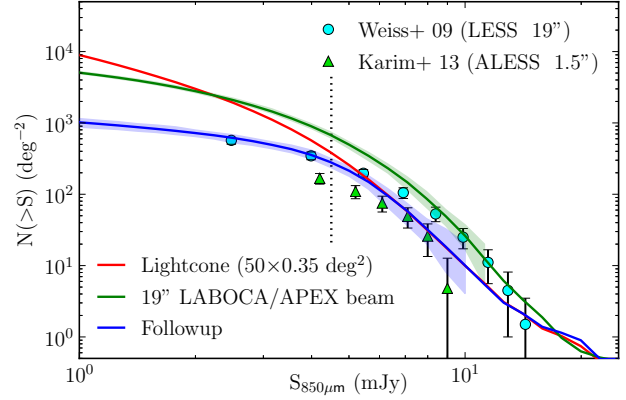


Figure 10. Comparison to (A)LESS number counts. The blue line is our prediction for our combined (17.5 deg^2) follow-up catalogues (described in text) and is to be compared to the ALESS number counts presented in Karim et al. (2013) (green triangles). The green line is our $19''$ source-extracted number counts for the combined (17.5 deg^2) field and is to be compared to the Weiß et al. (2009) number counts (cyan circles). The shaded regions indicate the 10-90 percentiles of the distribution of the individual (0.35 deg^2) field number counts. The red line is the number counts for the combined field from our lightcone catalogues. The vertical dotted line indicates the 4.5 mJy single-dish source-extraction limit of LESS.

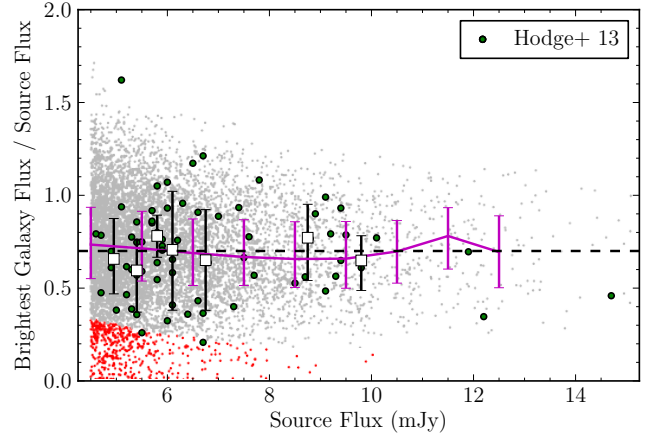


Figure 11. Ratio of brightest galaxy component flux to single-dish source flux. Grey scatter points show the brightest galaxies from our followed-up sources over our combined 17.5 deg^2 simulated field. Red points show where the brightest follow-up galaxy falls below the ALESS detection limit. The magenta line shows the median in a given flux bin with the errorbars indicating the interquartile range. Observational data is taken from the Hodge et al. (2013) ALESS catalogue. The white squares indicate the median observational flux ratio and source flux in a given bin, with the binning chosen such that there are roughly equal numbers of sources in each bin. Error bars indicate the 1σ percentiles of the ratio distribution in each observational bin. The black dashed line is a reference line drawn at 70% .

comparable to that seen observationally. Also plotted in Fig. 11 are sources for which the brightest galaxy is below the flux limit of ALMA (red points). These account for $\sim 5\%$ of our sources. Hodge et al. (2013) found that $\sim 19 \pm 4\%$ of the 88 ALMA ‘Good Maps’ did not contain a galaxy above the 1.5 mJy flux limit. The greater fraction of blank maps in the observational study could be caused by extended/diffuse SMGs falling below the detection threshold of ALMA.

⁶ We re-calculate the ‘effective’ area of our follow-up surveys according to $0.35 \text{ deg}^2 \times N_{\text{Good ALMA Maps}}/N_{\text{LESS Sources}} \approx 0.25 \text{ deg}^2$ as in Karim et al. (2013)

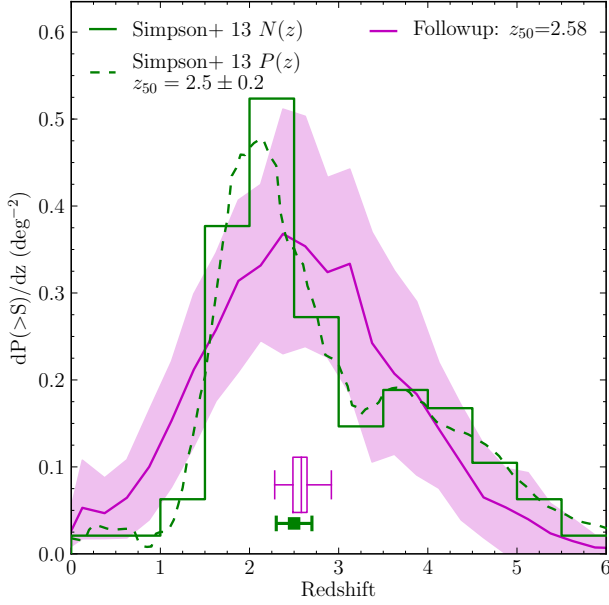


Figure 12. Comparison of normalised redshift distributions for the simulated and observed ALESS surveys. ALESS redshift distributions: a histogram of 96 individual redshifts (solid green line) and the redshift $P(z)$ (the sum of the photometric redshift probability distributions, dashed green line) from Simpson et al. (2013). These both 19 include H -band absolute magnitude modelled redshifts (see Simpson et al. (2013) for details). The square marker indicates the observational median redshift with associated errors. The magenta solid line is the distribution for our combined 17.5 deg^2 field with the shaded region showing the 10-90 percentiles of the distributions from our 50 individual fields. The boxplot shows the distribution of median redshifts for each of our 50 fields, the whiskers indicate the full range, with the box and line indicating the inter-quartile range and median respectively.

4.2 Redshift Distribution

One of the main advantages of the 99 ALMA sources identified in Hodge et al. (2013) is that the greater positional accuracy ($\sim 0.2''$) provided by ALMA allows accurate positions to be determined without introducing biases associated with selection at wavelengths other than sub-mm (e.g. radio). Simpson et al. (2013) derived photometric redshifts for 77 of 96 ALMA SMGs⁷. The remaining 19 were only detected in $\lesssim 3$ bands so no reliable photometric redshifts could not be determined. Redshifts for these ‘non-detections’ were modelled in a statistical way based on assumptions regarding the H -band absolute magnitude (M_H) distribution of the 77 ‘detections’ (see Simpson et al. (2013) for more details). We compare the redshift distribution presented in Simpson et al. (2013) both in terms of the histogram of individual galaxies (solid histogram) and the $P(z)$ ⁸ (dashed line), to our simulated follow-up survey in Fig. 12. We note that both of these observational distributions include the M_H modelled redshifts.

Our model reproduces the high redshift ($z > 4$) tail and is

⁷ Three of the 99 SMGs presented in Hodge et al. (2013) lay on the edge of E-CDFS and had coverage in only two IRAC bands so were not considered further in Simpson et al. (2013).

⁸ The sum of the individual photometric redshift probability distributions. This has the benefit of not being sensitive to histogram binning and includes information regarding the errors of the photometric redshift.

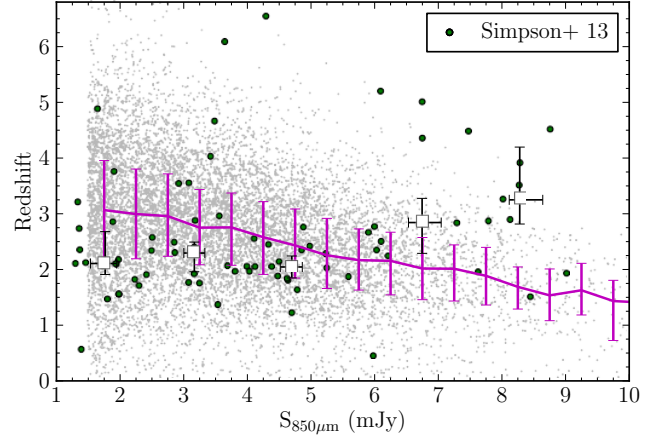


Figure 13. Relation between $S_{850\mu\text{m}}$ and redshift for our follow-up galaxies over our combined 17.5 deg^2 field. Solid line shows the median redshift in a given $1 \text{ mJy } S_{850\mu\text{m}}$ bin with errorbars indicating the inter-quartile range. Observational data from Simpson et al. (2013) has been binned in 2 mJy bins, with the median redshift plotted as the white squares with errorbars indicating 1σ bootstrap errors.

consistent with the median redshift of the observed distribution. We performed the K-S test between each of our 50 follow-up redshift distributions and the ALESS distribution. We find a low median p value of 0.176 with 12% of the K-S tests exhibiting $p < 0.05$. We do note however, that the M_H band modelling of the 19 ‘non-detections’ ($\sim 20\%$ of the sample), and the sometimes significant photometric errors may affect the overall observed distribution.

We also investigate whether or not our model reproduces the same behaviour as seen in ALESS between redshift and $S_{850\mu\text{m}}$ in Fig. 13. Our model predicts that at lower redshift our simulated SMG population is generally brighter whilst in the observational data the opposite appears to be the case. However, Simpson et al. (2013) argue that this trend in their data is not significant and that their non-detections, 14/19 of which are at $S_{870\mu\text{m}} < 2 \text{ mJy}$, would likely render it flat if redshifts could be determined for these galaxies.

5 MULTI-WAVELENGTH SURVEYS

Until now we have focussed on surveys performed at $850 \mu\text{m}$, traditionally the wavelength at which most sub-mm surveys have been performed. However, there are now a number of observational blank-field surveys performed at other sub-mm wavelengths (e.g. Scott et al. 2012; Chen et al. 2013; Geach et al. 2013). In this section we briefly investigate the effects of the finite single-dish beam-size at $450 \mu\text{m}$ ($\sim 8''$ FWHM e.g. SCUBA2/JCMT) and $1100 \mu\text{m}$ ($\sim 28''$ FWHM e.g. AzTEC/ASTE⁹). We add that due to our self-consistent dust model the results presented in this section are genuine multi-wavelength predictions and do not rely on applying an assumed fixed flux ratio.

We create lightcones as described in Section 2.3, taking the lower flux limit at which we include galaxies in our lightcone catalogue as the limit above which 90% of the EBL is resolved at that wavelength, as predicted by our model. This is $0.125 (0.02) \text{ mJy}$ at

⁹ Aztronomical Thermal Emission Camera/Atamaca Sub-millimetre Telescope Experiment

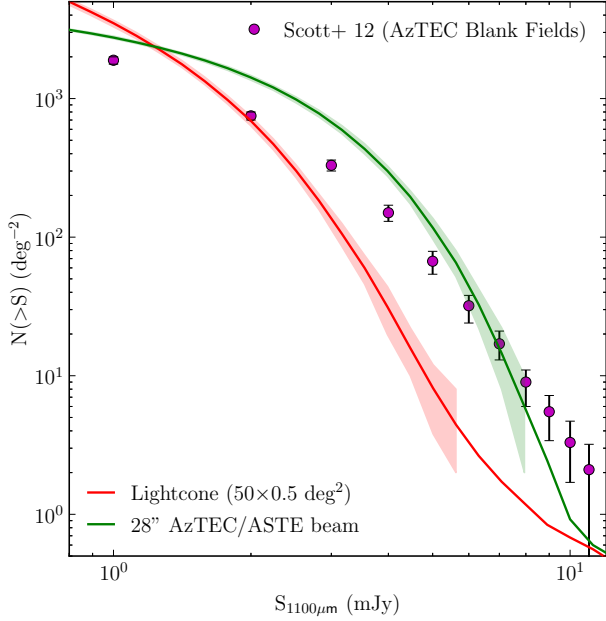


Figure 15. Predictions for cumulative blank-field single-dish number counts at $1100\ \mu\text{m}$. Number counts from our lightcone (red) and $28''$ FWHM beam source-extracted (green) catalogues are shown. The shaded regions are the 10-90 percentiles of our individual field number counts. Observational data is taken from Scott et al. (2012) (magenta circles).

$450\ (1100)\ \mu\text{m}$. As at $850\ \mu\text{m}$, our EBL predictions are in excellent agreement with observational data from the *COBE* satellite. We also follow the same procedure as described in Section 2.4 for creating our mock maps. However, we change the standard deviation of our Gaussian noise such that the match-filtered noise-only maps have a σ of $\sim 4\ (1)$ mJy/beam at $450\ (1100)\ \mu\text{m}$ to be comparable to published blank-field surveys at that wavelength (e.g. Aretxaga et al. 2011; Casey et al. 2013).

Thumbnails of the same area, but for different wavelength maps, are shown for comparison in Fig. 14. The effect of the beam size increasing with wavelength is clearly evident, as is the resulting multiplicity of some of the sources.

In Fig. 15 we present the $1100\ \mu\text{m}$ number counts from our source-extracted and lightcone catalogues. The observational data from Scott et al. (2012) is a combined sample of previously published number counts with a total area of $1.6\ \text{deg}^2$, $1.22\ \text{deg}^2$ of which was taken using the AzTEC/ASTE configuration. As at $850\ \mu\text{m}$, considering the effects of the finite beam-size brings the model into better agreement with the observational data.

The number counts at $450\ \mu\text{m}$ are presented in Fig. 16, we attribute the enhancement in our simulated source-extracted counts at $S_{450\mu\text{m}} \sim 8\ \text{mJy}$ to Eddington bias, caused by the instrumental noise rather than the effects of the $8''$ beam. In this case the source extracted counts derived from the astrophysical maps are much steeper at 2σ ($8\ \text{mJy}$ at $450\ \mu\text{m}$) than at $850\ \mu\text{m}$ as the beam size is smaller, so it is unsurprising we are affected more by Eddington bias here. In order to account for this we ‘deboost’ our $S_{450\mu\text{m}} > 5\ \text{mJy}$ sources following the method outlined in Casey et al. (2013). The total galaxy flux of each of our $S_{450\mu\text{m}} > 5\ \text{mJy}$ sources is calculated as described in Section 3.2 and we plot this as a ratio to source flux in Fig. 17. We multiply the flux of our $450\ \mu\text{m}$ sources by the median of this ratio before re-calculating the number counts (see dotted line in Fig. 16).

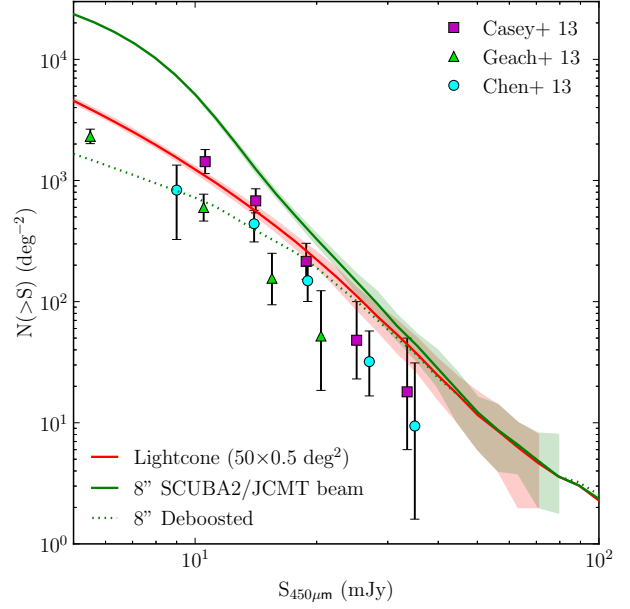


Figure 16. Predictions for cumulative blank-field single-dish number counts at $450\ \mu\text{m}$. Number counts from our lightcone (red) and $8''$ FWHM beam source-extracted (green) catalogues are shown for our combined $25\ \text{deg}^2$ field. The dotted green line shows the de-boosted source-extracted counts for the combined field (see text). The shaded regions show the 10-90 percentiles of our individual field number counts. Observational data is taken from Casey et al. (2013) (magenta squares), Geach et al. (2013) (green triangles) and Chen et al. (2013) (cyan circles).

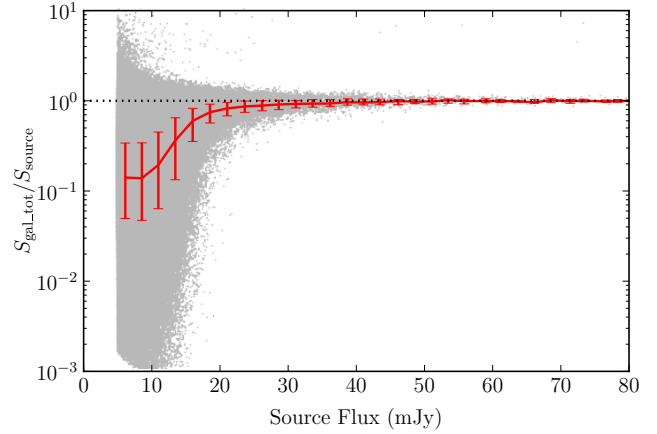


Figure 17. Ratio of total galaxy flux (see Section 3.2) to source flux at $450\ \mu\text{m}$. Red line and errorbars shows median and inter-quartile range in a given flux bin respectively.

6 SUMMARY

We present predictions for the effect of the coarse angular-resolution of single-dish telescopes, and field-to-field variations, on observations of SMGs. An updated version of the GALFORM semi-analytic galaxy formation model is coupled with a self-consistent calculation for the reprocessing of stellar radiation by dust. We use a sophisticated lightcone method to generate mock catalogues of SMGs out to $z = 8.5$ from which we create mock sub-mm maps following observational techniques. Sources are extracted from these mock maps to generate our source-extracted catalogue

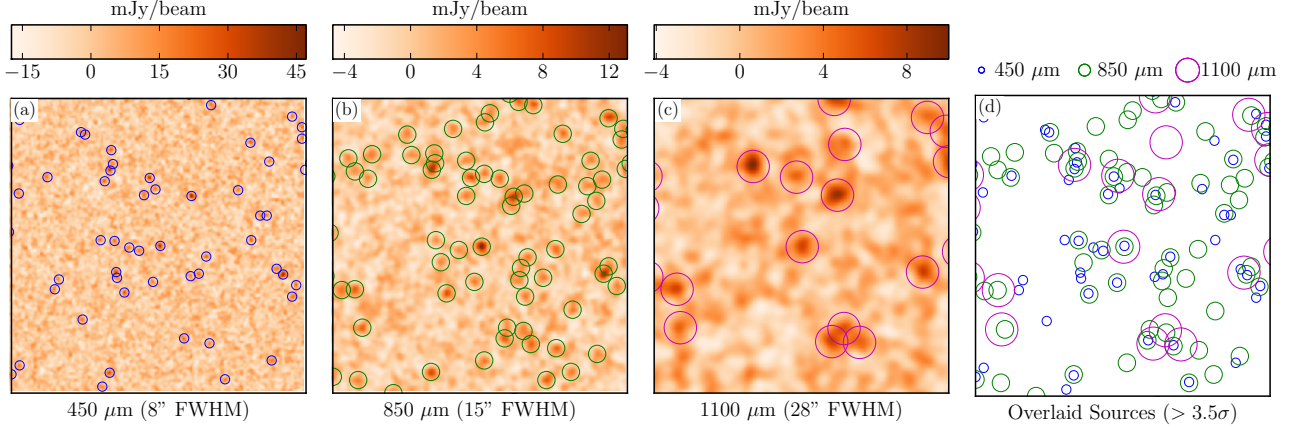


Figure 14. Thumbnails of the same $0.2 \times 0.2 \text{ deg}^2$ area as depicted in panels (a)-(d) of Fig. 3 but at (a) $450 \mu\text{m}$, (b) $850 \mu\text{m}$ and (c) $1100 \mu\text{m}$. Overlaid are the $> 3.5\sigma$ sources, as circles centred on the source position with a radius of $\sqrt{2} \times \text{FWHM}$ of the telescope beam at that wavelength. In (d) the $> 3.5\sigma$ sources at each wavelength are overlaid, without background for clarity.

and show the effects of the single-dish beam on the predicted number counts. To ensure a realistic background in our maps we include model SMGs down to the limit above which 90% of our total predicted EBL is resolved. Our model shows excellent agreement with EBL observations from the *COBE* satellite at 450 , 850 and $1100 \mu\text{m}$. We generate $50 \times 0.5 \text{ deg}^2$ randomly orientated surveys to investigate the effects of field-to-field variations.

The number counts from our $850 \mu\text{m}$ source-extracted catalogues display a significant enhancement over those from our light-cone catalogues at brighter fluxes ($S_{850\mu\text{m}} > 1 \text{ mJy}$) due to the sub-mm emission from multiple SMGs being blended by the finite single-dish beam into a single source. The field-to-field variations predicted from both catalogues for the $850 \mu\text{m}$ number counts are comparable to (or less than) quoted observational errors, for simulated surveys of 0.5 deg^2 area with a $15''$ FWHM beam ($\sim \text{SCUBA2/JCMT}$). Typically ~ 4 SMGs contribute 90% of the flux contributed to the source by galaxies, and this multiplicity slowly decreases with increasing flux over the range of fluxes investigated by blank-field single-dish surveys at $850 \mu\text{m}$. We find further that these blended galaxies are mostly physically unassociated i.e. their redshift separation implies that they are chance projections along the line of sight of the survey.

Our redshift distributions predict a median redshift of $z_{50} = 2$ for our ‘bright’ ($S_{850\mu\text{m}} > 5 \text{ mJy}$) population and $z_{50} = 2.8$ for our ‘faint’ ($S_{850\mu\text{m}} > 1 \text{ mJy}$) population. We leave these as predictions for blank field interferometric surveys of comparable area. We also observe that the field-to-field variations we predict for our bright population are comparable to those expected for Poisson errors whereas for our faint population the field-to-field variations are greater than Poisson.

A comparison between the ALESS survey and our model reveals that the model can reproduce the observed difference between single-dish and interferometer number counts. It can also reproduce the high redshift ($z > 4$) tail and median redshift of the observed photometric redshift distribution.

We also present predictions for our lightcone and source-extracted catalogue number counts at $450 \mu\text{m}$ and $1100 \mu\text{m}$ which show good agreement with the observational data and that the finite beam-size does not lead to a significant enhancement of the number counts at 450 , as opposed to 850 and $1100 \mu\text{m}$ as the beam-size at $450 \mu\text{m}$ is significantly smaller. Due to our dust model these are

genuine multi-wavelength predictions and do not rely on applying an assumed fixed flux ratio.

Our results highlight the importance of considering effects such as the finite beam-size of single-dish telescopes and field-to-field variance when comparing sub-mm observations with theoretical models. In our model SMGs are predominantly a disc instability triggered starburst population, the sub-mm emission of which is often blended along the line of sight of observational single-dish surveys.

In future work we will conduct a more thorough investigation of the properties and evolution of SMGs within the model presented in L14, including an analysis of their clustering with and without the effects of the single-dish beam. We hope that this, when compared to future observations aided by sub-mm interferometry of increasing sample sizes, will lead to a greater understanding of this extreme and important galaxy population.

ACKNOWLEDGMENTS

The authors would like to thank James Simpson and Chian-Chou Chen for helpful discussions. This work was supported by the Science and Technology Facilities Council [grant numbers, ST/K501979/1, ST/F001166/1]. This work used the DiRAC Data Centric system at Durham University, operated by the Institute for Computational Cosmology on behalf of the STFC DiRAC HPC Facility (www.dirac.ac.uk). This equipment was funded by BIS National E-infrastructure capital grant ST/K00042X/1, STFC capital grant ST/H008519/1, and STFC DiRAC Operations grant ST/K003267/1 and Durham University. DiRAC is part of the National E-Infrastructure.

REFERENCES

- Aretxaga I., Wilson G. W., Aguilar E., et al., 2011, *MNRAS*, 415, 3831
- Baugh C. M., 2006, *Rep. Progress Phys.*, 69, 3101
- Baugh C. M., Lacey C. G., Frenk C. S., et al., 2005, *MNRAS*, 356, 1191
- Benson A. J., 2010, *Phys. Rep.*, 495, 33

- Biggs A. D., Ivison R. J., Ibar E., et al., 2011, *MNRAS*, 413, 2314
- Blain A. W., Jameson A., Smail I., et al., 1999, *MNRAS*, 309, 715
- Blain A. W., Smail I., Ivison R. J., Kneib J.-P., Frayer D. T., 2002, *Phys. Rep.*, 369, 111
- Blaizot J., Wadadekar Y., Guiderdoni B., et al., 2005, *MNRAS*, 360, 159
- Blitz L., Rosolowsky E., 2006, *ApJ*, 650, 933
- Bower R. G., Benson A. J., Malbon R., et al., 2006, *MNRAS*, 370, 645
- Casey C. M., Chen C.-C., Cowie L. L., et al., 2013, *MNRAS*, 436, 1919
- Casey C. M., Narayanan D., Cooray A., 2014, *ArXiv e-prints*
- Chapin E. L., Chapman S. C., Coppin K. E., et al., 2011, *MNRAS*, 411, 505
- Chapman S. C., Blain A. W., Smail I., Ivison R. J., 2005, *ApJ*, 622, 772
- Chen C.-C., Cowie L. L., Barger A. J., et al., 2013, *ApJ*, 776, 131
- Cole S., Lacey C. G., Baugh C. M., Frenk C. S., 2000, *MNRAS*, 319, 168
- Coppin K., Chapin E. L., Mortier A. M. J., et al., 2006, *MNRAS*, 372, 1621
- Devriendt J. E. G., Guiderdoni B., 2000, *A&A*, 363, 851
- Draine B. T., Lee H. M., 1984, *ApJ*, 285, 89
- Fixsen D. J., Dwek E., Mather J. C., Bennett C. L., Shafer R. A., 1998, *ApJ*, 508, 123
- Geach J. E., Chapin E. L., Coppin K. E. K., et al., 2013, *MNRAS*, 432, 53
- Granato G. L., Lacey C. G., Silva L., et al., 2000, *ApJ*, 542, 710
- Hayward C. C., Behroozi P. S., Somerville R. S., et al., 2013, *MNRAS*, 434, 2572
- Hayward C. C., Narayanan D., Kereš D., et al., 2013, *MNRAS*, 428, 2529
- Helly J. C., Cole S., Frenk C. S., et al., 2003, *MNRAS*, 338, 903
- Hodge J. A., Karim A., Smail I., et al., 2013, *ApJ*, 768, 91
- Hughes D. H., Serjeant S., Dunlop J., et al., 1998, *Nat*, 394, 241
- Jiang L., Helly J. C., Cole S., Frenk C. S., 2014, *MNRAS*, 440, 2115
- Karim A., Swinbank A. M., Hodge J. A., et al., 2013, *MNRAS*, 432, 2
- Kennicutt Jr. R. C., 1983, *ApJ*, 272, 54
- Komatsu E., Smith K. M., Dunkley J., et al., 2011, *ApJS*, 192, 18
- Lagos C. D. P., Lacey C. G., Baugh C. M., Bower R. G., Benson A. J., 2011, *MNRAS*, 416, 1566
- Laurent G. T., Aguirre J. E., Glenn J., et al., 2005, *ApJ*, 623, 742
- Merson A. I., Baugh C. M., Helly J. C., et al., 2013, *MNRAS*, 429, 556
- Michałowski M. J., Dunlop J. S., Ivison R. J., et al., 2012, *MNRAS*, 426, 1845
- Mo H. J., Mao S., White S. D. M., 1998, *MNRAS*, 295, 319
- Parkinson H., Cole S., Helly J., 2008, *MNRAS*, 383, 557
- Puget J.-L., Abergel A., Bernard J.-P., et al., 1996, *A&A*, 308, L5
- Scott K. S., Wilson G. W., Aretxaga I., et al., 2012, *MNRAS*, 423, 575
- Silva L., Granato G. L., Bressan A., Danese L., 1998, *ApJ*, 509, 103
- Simpson J., Swinbank M., Smail I., et al., 2013, *ArXiv e-prints*
- Smail I., Ivison R. J., Blain A. W., 1997, *ApJL*, 490, L5
- Smolčić V., Aravena M., Navarrete a., 2012, *A&A*, 548, A4
- Springel V., White S. D. M., Jenkins A., et al., 2005, *Nat*, 435, 629
- Stetson P. B., 1987, *PASP*, 99, 191
- Swinbank A. M., Lacey C. G., Smail I., et al., 2008, *MNRAS*, 391, 420
- Vieira J. D., Crawford T. M., Switzer E. R., et al., 2010, *ApJ*, 719, 763
- Vieira J. D., Marrone D. P., Chapman S. C., et al., 2013, *Nat*, 495, 344
- Wang W.-H., Cowie L. L., Barger A. J., Williams J. P., 2011, *ApJL*, 726, L18
- Weiβ A., Kovács A., Coppin K., et al., 2009, *ApJ*, 707, 1201